

Black Hole Mergers From Globular Clusters Observable by LISA II: Resolved Eccentric Sources and the Gravitational Wave Background

Daniel J. D’Orazio^{1*}, Johan Samsing²

¹*Department of Astronomy, Harvard University, 60 Garden Street Cambridge, MA 01238, USA*

²*Department of Astrophysical Sciences, Princeton University, Peyton Hall, 4 Ivy Lane, Princeton, NJ 08544, USA*

19th October 2018

ABSTRACT

In paper I of this series we showed that a large percentage of the binary black hole (BBH) mergers that form through dynamical interactions in globular clusters will have significant eccentricity in the $\sim 10^{-3} - 10^{-1}$ Hz LISA band. In this work we quantify the evolution of these highly eccentric binaries through the LISA and LIGO bands, and compute the stochastic gravitational wave background from the merging, eccentric population. We find that the population of BBHs that merge in-between three-body encounters inside their cluster ($\sim 50\%$ of all cluster-formed BBH mergers) will have measurable eccentricity for their entire lifetime in the LISA band. The population of BBHs that merge during three-body encounters ($\sim 5\%$ of all cluster-formed BBH mergers), will be detectable by LIGO with eccentricities of $e \sim 0.1$. The gravitational wave background from dynamically assembled BBHs encodes a characteristic bump due to the high initial eccentricities of these systems. The location and amplitude of this bump depends on globular cluster properties.

Key words: gravitational waves, stars: black holes, galaxies: star clusters: general

1 INTRODUCTION

The Laser Interferometer Gravitational Wave Observatory (LIGO) is beginning to reveal the population of stellar-mass black holes (BHs) that come together and merge within a Hubble time (Abbott et al. 2016b,e,a, 2017a,c,b). To varying degrees of accuracy, LIGO can measure BH masses, spins, mass ratios, and eccentricities (e.g. Abbott et al. 2016f,d). The distribution of these parameters for binary black holes (BBHs) at merger will help to quantify the population of BBHs in the universe, and begin to teach us about the origin of these systems (e.g., O’Leary et al. 2009; Kocsis & Levin 2012; Samsing et al. 2014; Breivik et al. 2016; Rodriguez et al. 2016b; Farr et al. 2017; Zevin et al. 2017; Samsing & Ramirez-Ruiz 2017; Samsing & Ilan 2017; Samsing 2017; Belczynski et al. 2017; Samsing et al. 2018b; Farr et al. 2018).

LIGO, however, is sensitive only to the final seconds of a BBH inspiral and merger, at gravitational wave (GW) frequencies of 10’s of Hz to kHz. The final inspiral and merger generates the highest amplitude GWs, and is arguably the most interesting portion of a BBH merger from a gravitational perspective, encoding tests of gravity in the strong field (Lehner & Pretorius 2014; Abbott et al. 2016c; Yunes et al. 2016). Astrophysically, however, it is only a small snapshot of the BBH lifetime. While precessional dynam-

ics, as well as combinations of mass, redshift, and effective spin measurements of BBHs measured in the LIGO band can encode aspects of formation mechanisms (see, e.g., Gerosa et al. 2013; Kesden et al. 2015; Gerosa et al. 2015; Rodriguez et al. 2016b; Gerosa & Berti 2017; Rodriguez et al. 2017; Fishbach et al. 2017), many of the astrophysical imprints on formation are washed away by the dissipative effects of the gravitational radiation reaction that brings the binary to coalescence.

A fuller understanding of the processes that govern the formation and inspiral of BBH systems merging in the LIGO band requires a census of the BBHs earlier in their lifetimes, when imprints of formation could be strong. One such imprint, which is rapidly erased by GW emission later in the BBH evolution, is binary eccentricity (e.g., Gondán et al. 2018). BBHs formed via dynamical assembly are expected to have non-zero eccentricity (Benacquista 2002; O’Leary et al. 2009; Kocsis & Levin 2012; Samsing et al. 2014; Cholis et al. 2016; Samsing & Ramirez-Ruiz 2017; Samsing & Ilan 2017; Samsing 2017; Rodriguez et al. 2017; Gondán et al. 2017; Samsing et al. 2018b; Samsing & Ilan 2018; Samsing et al. 2018c; Randall & Xianyu 2018b,a) in contrast with BBHs formed near zero eccentricity in the field, with the exception of field BBHs that are driven to merger through secular evolution (e.g., Silsbee & Tremaine 2017; Randall & Xianyu 2018b,a). Higher eccentricity causes a binary with otherwise the same orbital frequency to merge in a shorter time (Peters 1964). Higher eccentricity also causes a

* daniel.dorazio@cfa.harvard.edu; jsamsing@princeton.edu

binary to emit GWs at a spread of GW frequencies that are peaked at a higher harmonic of its orbital frequency than for a binary on a circular orbit, which emits GWs only at the second harmonic of its orbital frequency (e.g., [Peters & Mathews 1963](#)).

Interestingly, a subset of the BBH mergers detectable by LIGO will also be detectable earlier in their evolution by the Laser Interferometer Space Antennae (LISA; [Amaro-Seoane et al. 2017](#)), at lower GW frequencies, $\sim 10^{-2}$ Hz (see [Fregeau et al. 2006](#); [Amaro-Seoane & Santamaría 2010](#); [Sesana 2016](#); [Seto 2016](#), and references therein). Hence, while LIGO will continue to detect BBHs at merger, LISA holds the exciting prospect of detecting the same BBHs closer to formation, providing key information for distinguishing BBH formation channels ([Nishizawa et al. 2016](#); [Breivik et al. 2016](#); [Nishizawa et al. 2017](#); [Samsing & D’Orazio 2018](#)). If the proposed DECIGO ([Kawamura et al. 2011](#)) or Tian Qin ([Luo et al. 2016](#)) detectors succeed in filling in the GW frequency gap between LISA and LIGO, then for some systems, the majority of the BBH evolution can be tracked from near formation to merger (e.g., [Samsing et al. 2018a](#)).

In [Samsing & D’Orazio \(2018\)](#) (hereafter Paper I) we discussed the mechanisms by which three different channels for the formation of BBHs in globular clusters (GCs) lead to three distinct modes in the distribution of binary eccentricities, and hence distinct GW peak frequencies at formation for each channel. The three types of BBH mergers resulting from dynamical formation in GCs are

- The *ejected mergers*: occurring for BBHs that are hardened over a series of binary-single interactions until they are sufficiently tightly bound that the next binary-single interaction results in ejection of the BBH from the GC (e.g., [Rodríguez et al. 2016a](#); [Park et al. 2017](#); [Samsing 2017](#)). If the ejected BBH has high enough eccentricity at ejection it will merge in a Hubble time ([Portegies Zwart & McMillan 2000](#); [Rodríguez et al. 2016a](#); [Samsing 2017](#)). In the following we loosely refer to an ejected merger as an ejected BBH that merges within a Hubble time and contributes to the present day observable BBH mergers.

- The *2-body in-cluster* (hereafter ‘2-body’) mergers: occurring when a BBH has high enough eccentricity to merge in-between binary-single interactions, before being ejected from the GC ([Samsing 2017](#); [Rodríguez et al. 2017](#)).

- The *3-body in-cluster* (hereafter ‘3-body’) mergers: occurring when a BBH is formed in a binary-single interaction with such high eccentricity that a ‘GW capture’ merges the binary in the GC, before the third body can disrupt the orbit ([Gültekin et al. 2006](#); [Samsing et al. 2014](#)).

In Paper I, we showed that the ejected mergers form with eccentricities above ~ 0.85 and orbital frequencies of $\sim 10^{-7}$ Hz. High eccentricity causes the GW emission to be emitted primarily at higher harmonics of the orbital frequency than for a circular orbit, at $\sim 10^{-4} - 10^{-5}$ Hz, just below the minimum frequencies that can be probed by the LISA band. On the other extreme, the 3-body mergers form with similar orbital frequencies, but such high eccentricity $e \sim 0.9999$ that their initial GW frequencies peak high of the LISA band, at $1 - 10$ Hz ([Chen & Amaro-Seoane 2017](#); [Samsing et al. 2018a](#)). The 2-body mergers form with eccentricity intermediate to the ejected and 3-body mergers, causing their peak GW frequency at formation to fall directly in the LISA band (Paper I).

In this work, we quantify the evolution of orbital eccentricity and GW emission of these three BBH populations. In §2 We compute the eccentricity evolution, characteristic GW strain, and corresponding signal-to-noise ratios of representative BBHs from each

of the three eccentric populations in the LISA and LIGO bands. We show that LISA will be able to measure the eccentricity of the 2-body BBH population, distinguishing it from the ejected merger population that has a lower average eccentricity, marginally measurable by LISA, and from the 3-body population, which LISA will not detect [Samsing et al. \(2018a\)](#). We also show that the 3-body population will have a measurable eccentricity in LIGO, meaning that LISA and LIGO observations should be able to disentangle the three dynamical formation channels discussed here. Beyond individually resolvable sources, we present in §3 a calculation of the stochastic gravitational wave background from these dynamically formed BBH populations, including a full treatment of binary eccentricity. Finally, in §4, we explore the dependence of our findings on GC properties, specifically the escape velocity from the cluster.

2 ORBITAL EVOLUTION AND GW EMISSION FROM INDIVIDUALLY RESOLVED BBHS

In this section we quantify the orbital evolution of the dynamically assembled BBH populations and determine their detectability as individually resolved sources in LISA and LIGO. The calculations presented here take as input the initial masses, orbital frequencies and eccentricity distributions of BBHs formed dynamically in GCs. These distributions are derived in Paper I of this series with the following assumptions. We assume that all BHs have a mass of $30M_{\odot}$, so that the BBHs have total masses of $60M_{\odot}$. This is a simplifying assumption motivated by the propensity for dynamically formed systems to form near equal mass, high mass binaries ([Rodríguez et al. 2016a](#)), and by half of the LIGO BBHs having a similar make-up (e.g., [Zevin et al. 2017](#)). Unless otherwise stated, we choose for the fiducial GC properties, an escape velocity of $v_{\text{esc}} = 50 \text{ km s}^{-1}$ and a core single-BH density of $n_s = 10^5 \text{ pc}^{-3}$. Further details are available in Paper I.

2.1 Eccentricity evolution

We first consider the GW-driven eccentricity evolution of a representative BBH from each population. Figure 1 shows the binary eccentricity evolution for each of the three populations: ejected (blue), 2-body (green), and 3-body (red). Each assumes purely GW-driven orbital evolution ([Peters 1964](#)), and the population average initial orbital frequencies and eccentricities ($\langle e_0 \rangle$, $\langle f_{\text{orb},0} \rangle$) supplied by Paper I. The solid lines track eccentricity vs. the rest-frame orbital frequency (f_{orb}) while the dashed lines track eccentricity vs. the peak rest-frame *gravitational wave* frequency, which we approximate as¹

$$f_r^{\text{peak}} \approx 2f_{\text{orb}}(1-e)^{-3/2}. \quad (1)$$

The filled circles denote the population average $\langle e_0 \rangle$ and $\langle f_{\text{orb},0} \rangle$ at formation. BBHs from each formation channel effectively form with the same initial orbital frequency, corresponding approximately to the semi-major axis below which a subsequent binary-single interaction would eject the BBH from the cluster. The differences in the eccentricity evolution between each BBH population is due primarily to the different initial eccentricities of each population, which is regulated by the merger timescale for each

¹ This is simply the orbital frequency if the binary had semi-major axis equal to its pericentre distance. This is very similar to other, slightly more complicated, approximations used in the literature (e.g., [Wen 2003](#)).

formation channel. Because binaries on highly eccentric orbits emit most of their GW power in high harmonics of the orbital frequency (see §2.2), differences in initial eccentricity results in the very different initial peak GW frequencies denoted by the stars in Figure 1.

To see how the characteristic peak frequency at formation, of a given population with merger time scale \mathcal{T} , scales with the BBH orbital parameters, one can combine the expression for the GW inspiral lifetime $\mathcal{T} \approx t_c(1 - e^2)^{7/2}$ (see, e.g., Peters (1964)), where t_c denotes the circular-orbit lifetime and e is the eccentricity, with the relation for f_r^{peak} given by Eq. (1), to find,

$$f_{r,0}^{\text{peak}}(\mathcal{T}) \approx 2 \cdot 10^{-5} \text{ Hz} \left(\frac{\mathcal{T}}{10^{10} \text{ yrs}} \right)^{-3/7} \left(\frac{a}{0.5 \text{ au}} \right)^{3/14} \left(\frac{m}{30 M_\odot} \right)^{-11/14} \quad (2)$$

The characteristic time scales for our three considered populations, ejected mergers, 2-body mergers, and 3-body mergers, are the Hubble time ($t_H \sim 10^{10}$ yrs), the binary-single encounter time ($\sim 10^7$ yrs), and the BBH orbital time (~ 0.1 yr), respectively. Substituting these time limits into Eq. (2), one finds that the three corresponding characteristic peak frequencies are $\log f_{r,0}^{\text{peak}} \approx -4.5$ (ejected BBH mergers), $\log f_{r,0}^{\text{peak}} \approx -3.5$ (2-body BBH mergers), and $\log f_{r,0}^{\text{peak}} \approx 0$ (3-body BBH mergers). These frequencies roughly correspond to average initial eccentricities for each population of $\langle e_0 \rangle \approx 1 - 10^{-1}$ (ejected), $\langle e_0 \rangle \approx 1 - 10^{-2}$, (2-body), and $\langle e_0 \rangle \approx 1 - 10^{-5}$ (3-body). In other words, the three different populations that we find to have very different eccentricities in LIGO and LISA, are regulated simply by the time scale for each to undergo a merger. More detailed numerical simulations will undoubtedly find slight changes to the shape of the distributions, but the locations of $f_{r,0}^{\text{peak}}$ are robustly set by the three listed time scales, each of which can be straight forwardly estimated².

As the binaries evolve towards higher orbital frequencies due to gravitational radiation reaction, eccentricity is damped and the dashed lines in Figure 1 approach a value that is a factor of two greater in frequency than the solid lines. This is the usual factor of two relating the Keplerian orbital frequency and the GW frequency for binaries on circular orbits; binaries on circular orbits emit all of their GW power in the $n = 2$ harmonic.

Figure 1 also shows the LISA sensitivity from Cornish & Robson (2018) shaded as a function of GW frequency in orange, dark orange being the most sensitive. Also plotted are horizontal dotted lines, above which LISA can measure the binary eccentricity. For $e > 0.01$, LISA is expected to measure a non-zero eccentricity for all resolved BBHs, while for $e \sim 0.001$, LISA should detect non-zero eccentricity for $\sim 90\%$ of identified BBHs over a 5 year mission (Nishizawa et al. 2016; Seto 2016). The black-dotted vertical line denotes the peak GW frequency at which the ejected and 2-body populations will have approximately a 5 year lifetime until merger, at $z = 0.1$ (see Eq. 8). Hence, only the BBHs with frequencies to the right of the black-dotted line (when a 5 year LISA mission begins) are accessible to both LISA and LIGO.

² The least known time scale is the encounter time scale, which is set by the number density of single BHs in the GC core, n_s ; a number that at present is highly uncertain. However, as described in §4, both the location of the 2-body GW peak frequency and its normalization depends only weakly on n_s , and an order-of-magnitude uncertainty in n_s does therefore not impact our results significantly.

The ejected BBHs enter the LISA band with detectable eccentricity of $e \sim 0.01$, but circularize below $e \sim 0.001$ by the time they reach the frequency above which a BBH will merge during the LISA mission lifetime. Hence, BBHs in the ejected population that will be detectable by LISA and LIGO have eccentricity that is only marginally measurable by LISA.

The majority of the 2-body BBHs form with peak GW power in the LISA band and remain above $e = 0.001$ for their entire voyage through the LISA band. Hence, binaries from this population, which is of order 50% of all BBH mergers dynamically assembled in GCs (Paper I), will have eccentricity detectable by LISA.

We note that Breivik et al. (2016) present a similar eccentricity evolution plot in their Figure 1, in which they consider only tracks of BBHs formed *without including* relativistic effects (GW radiation in the N -body equation-of-motion) considered in Paper I. We point out here that the *inclusion* of relativistic effects leads to the 2-body BBHs that are absent from the plot in Breivik et al. (2016) and have eccentricity such that they emit at peak GW frequencies directly in the LISA band (Paper I). Although relativistic effects occur at higher order in the N -body equation-of-motion for interactions in classical GCs, the 2-body mergers are not sub dominant, as they constitute up to about $\sim 50\%$ of all the BBH cluster mergers (Rodríguez et al. 2017; Samsing 2017; Samsing & D’Orazio 2018). This is a result of classical hardening, which gives each BBH repeated ‘tries’ for undergoing a merger inside the GC before ejection is possible (e.g., Samsing 2017).

Finally the 3-body BBHs are never prominent in the LISA band, rather, they are so eccentric that they will form in the region of GW-frequency space between LISA and LIGO (e.g., Chen & Amaro-Seoane 2017; Samsing et al. 2018a), and enter the LIGO band with $e \sim 0.1$ (e.g., Samsing 2017). These highly eccentric BBHs are the relevant population for the work by Chen & Amaro-Seoane (2017); Samsing et al. (2018a), who point out that very high eccentricity BBHs will have strain that is too low to be detected by LISA, but would be detectable by proposed GW detectors such as DECIGO (Kawamura et al. 2011) and Tian Qin (Luo et al. 2016) in the $\sim 1 - 10$ Hz band.

We now compute the tracks of binaries from each population in GW amplitude vs. GW frequency through the LISA band down to merger. This will tell us when the BBHs are detectable and the relevant eccentricities to which LISA and LIGO have access for each population.

2.2 Gravitational wave amplitudes

We have shown that the three BBH populations considered here exhibit an interesting range of eccentricities in the LISA and LIGO bands. We now wish to show that BBHs with these eccentricities and orbital frequencies will be detectable as individually resolved sources by LISA or LIGO. To do this we compute the characteristic strain of a representative BBH from each of the populations discussed above. We also compute the signal-to-noise ratio (S/N) of each eccentric BBH population in the LISA or LIGO band.

To compute the characteristic strain vs. GW frequency, $h_c(f)$, during the orbital evolution of an eccentric binary, we must consider the wide range of harmonics at which an eccentric binary emits gravitational waves. The n^{th} harmonic is emitted at a rest-frame GW frequency of $f_r = n f_{\text{orb}}$, where f_{orb} is the rest frame orbital frequency of the binary and the rest-frame and observed GW frequency are related through the cosmological redshift z , $f_r = (1 + z)f$. For a binary on a circular orbit, all power is emitted at the $n = 2$ harmonic, but in general, the characteristic strain

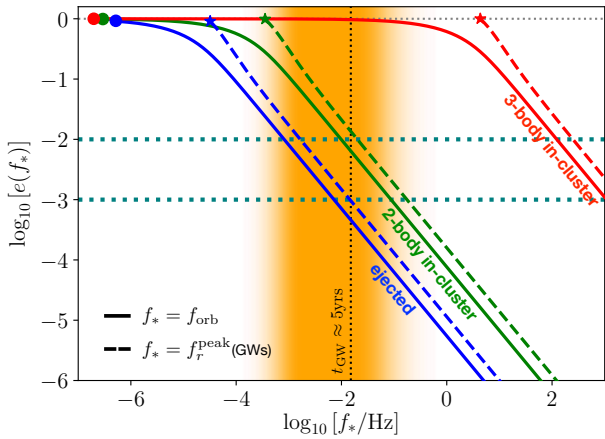


Figure 1. The eccentricity evolution of the three BBH populations discussed here and in Paper I, assuming a GC with an escape velocity of 50 km s^{-1} . We track representative BBHs from each population by using the average initial eccentricity and orbital frequency for each population. The solid lines represent the eccentricity as a function of binary orbital frequency, while the dashed lines plot the eccentricity vs. the (peak) gravitational wave frequency at which the most power is emitted. The circles denote the average eccentricity and orbital frequency at which the binaries form and the stars indicate the corresponding frequency of peak GW emission at formation. The orange shading represents the relative LISA sensitivity (darkest orange is the highest sensitivity) and the dashed, horizontal lines are the values above which LISA can measure the eccentricity of a resolved source in two different cases (see text). The vertical dotted line denotes the frequency above which BBHs at $z = 0.1$ will be observed to merge within the timescale of the 5 year LISA mission. As seen, the ejected mergers drift into the LISA band with eccentricities of ~ 0.01 . The 2-body mergers appear in the LISA band with eccentricities of nearly unity and leave with eccentricities above $\sim 10^{-3}$. The 3-body mergers appear outside of the LISA band.

in GWs at the n^{th} harmonic of the orbital frequency is (Barack & Cutler 2004),

$$h_{c,n}(f) = \frac{1}{\pi D} \sqrt{\frac{2G}{c^3} \frac{dE_n}{df_r}}, \quad (3)$$

where D is the luminosity distance to the source. The energy emitted per GW frequency at the n^{th} harmonic is given by (Enoki & Nagashima 2007; Huerta et al. 2015; Chen et al. 2017),

$$\frac{dE_n}{df_r} = \frac{(GM)^{5/3}}{3\pi^{1/3}(1+z)^{1/3}f^{1/3}} \left(\frac{2}{n}\right)^{2/3} \frac{g(n,e)}{F(e)}, \quad (4)$$

where $M \equiv Mq^{3/5}/(1+q)^{6/5}$ is the chirp mass for a binary with total mass $M = M_1 + M_2$ and mass ratio $q \equiv M_2/M_1 \leq 1$. The functions $g(n,e)$ and $F(e)$ are defined in Peters & Mathews (1963).

The above expression requires evaluation of the eccentricity at all points along the binary evolution. This is found by solving (e.g., Enoki & Nagashima 2007; Huerta et al. 2015),

$$\frac{f_{\text{orb}}}{f_0} = \left[\frac{1 - e_0^2}{1 - e^2} \left(\frac{e}{e_0}\right)^{12/19} \left(\frac{1 + \frac{121}{304}e^2}{1 + \frac{121}{304}e_0^2}\right)^{870/2299} \right]^{-3/2}, \quad (5)$$

at a specified orbital frequency, given the initial binary orbital frequency and eccentricity.

Because we are considering BBH sources with lifetimes that can be much longer than the LISA mission lifetime, we must adjust the characteristic strain to take into account this finite observation

lifetime in the LISA band, τ . This is primarily because the characteristic strain is a measure of the signal per frequency bin, and in the case of BBH sources, one must take into account the amount of time that a BBH spends in a given frequency bin compared to the total observation time. To do so, observe that the energy produced by a GW source at a given frequency is proportional to the squared GW strain h^2 times the number of cycles emitted at that frequency. Hence for comparing to the LISA/LIGO sensitivity curves, we compute the characteristic strain, $h_c(f) \equiv h(f)\sqrt{N} \propto h(f)\sqrt{f^2/\dot{f}}$, where \dot{f} is the rate of change of the binary frequency, making N the number of cycles spent in the frequency interval Δf (Sesana et al. 2005, our Eq. 3). When the number of cycles per frequency interval is larger than the total number of cycles observed at that frequency, in an observation time τ , the value of N in the characteristic strain becomes simply $f\tau$, and the total signal is set by how long LISA can gather signal in that frequency bin. In Figures 2 and 3 below, the characteristic strain is computed to take into account a finite observation time $\tau = 5$ years unless otherwise specified.

Each panel in Figure 2 shows the full GW emission from eccentric BBHs over their entire lifetimes. From left to right, we plot a representative BBH track from the ejected, 2-body, and 3-body BBH populations using the same mean initial orbital frequency and eccentricity as in Figure 1. In each panel, the solid black and grey lines are the sensitivity curves for the LISA and LIGO instruments respectively. To elucidate the binary evolution, we draw thick dashed lines for each population that trace the GW frequency of peak GW emission. The thin solid lines of a given color (blue, green, red) represent the GW-emission at a fixed binary orbital frequency, at a snapshot in the binary’s evolution.

The ‘knee’ in the BBH evolution tracks for the ejected and 2-body BBHs, occurring at $f \sim 10^{-1.8} \text{ Hz}$ (where the thin and thick dashed lines meet), is the transition between observation-duration limited and binary-inspiral limited characteristic strain. Practically, BBHs emitting at peak GW frequencies to the right of this knee, when LISA turns on, will merge during the mission lifetime, while those with starting frequency low of the knee will have negligible motion through frequency space as seen in Figure 2. A thin dashed line is drawn for reference to show the evolution of the characteristic strain over an infinite observation time.

Early in the evolution, the GW emission is much lower than what is expected for a circular-orbit binary at the same orbital frequency. This is because the binary is emitting a large spread of GW frequencies above its orbital frequency, resulting in the GW emission profile traced out by the solid colored lines. As the binary orbital frequency and eccentricity evolve, this profile becomes narrower, and higher in amplitude. In the early stage of evolution, when the binary is still very eccentric, the frequency of peak GW emission changes very little while the amplitude of emission increases rapidly. Eventually, the binary circularizes and the GW emission profile approaches a delta-function with peak at GW frequency tracking twice the binary orbital frequency.

The thick dashed lines tracing peak GW emission approximately follow the spine of the time series of constant f_{orb} emission profiles. At circularization, each track joins the $f^{-1/6}$ power law evolution expected for a BBH on a circular orbit (this power law would be extended to low frequencies for a binary initially on a circular orbit). This coincides with the point where the dashed and solid lines become parallel in Figure 1. The cutoff in characteristic strain at high frequencies signifies merger, where the orbital period is above the maximum plunge frequency (Barack & Cutler 2004).

Each line of constant orbital frequency is made up from the contribution of GWs at many harmonics of the orbital frequency;

the higher the eccentricity, the more harmonics contribute. To show this, the lighter colored markers connected by a thin line in each panel of Figure 2 denote the evolution of three selected harmonics of the GW emission. The ‘*’s pick out the $n = 2$ harmonic over the course of the binary evolution, while the ‘x’'s and filled circles represent higher harmonics as labeled. It is clear that the $n = 2$ harmonic rises to dominate over the higher order harmonics as the binary circularizes.

From left to right, the effect of a larger initial eccentricity can be readily observed. The middle and right panels exhibit a longer low frequency tail of GW emission early in the binary evolution. The higher eccentricity cases also sit at a nearly constant, and higher peak GW frequency for a larger range of characteristic amplitudes before circularizing, at which point the GW emission follows the orbital frequency to higher values and merger. In the right panel, the initial eccentricity is so high that the solid lines of constant orbital frequency near formation cannot be completed with the 100,000 harmonics included in this rendering. This manifests in the incomplete solid red lines at ~ 1 Hz and below $h_c \sim 10^{-25}$.

It is interesting to note that if the representative 3-body BBH studied here is at least twice as massive and within 10 Mpc, or instead consists of intermediate mass BHs at cosmological distance, the spread of emitted GWs, at a single point in time, spans both LISA and LIGO simultaneously. Such simultaneous multiband detection was pointed out by (Kocsis & Levin 2012), who have computed similar eccentric GW emission tracks for a different dynamical formation scenario.

In Figure 3 we summarize the tracks of GW emission of the three BBH populations, plotting only the evolution of the peak harmonic, $h_c(f^{\text{peak}})$. The thick lines show the peak characteristic strain assuming a LISA lifetime of 5 years, while, for reference, the thin lines show the peak characteristic strain assuming an infinite observation time. The thin lines are the same peak harmonic tracks as those plotted in Figure 2, for the fiducial GC parameters ($v_{\text{esc}} = 50 \text{ km s}^{-1}$). To show the dependence on GC properties, the dashed lines show the tracks of representative BBHs from each population coming instead from a GC with $v_{\text{esc}} = 20 \text{ km s}^{-1}$. Dependence on GC properties is discussed below in §4.

On the top x-axis of Figure 3 we quantify the length of a the binary track through GW frequency space over the course of a 5 year LISA mission. For a figure of merit we use the number of cycles observed at frequency f in the observing time τ divided by the approximate number of cycles that a binary spends at frequency f , f^2/\dot{f} (see e.g., Sesana et al. 2005), where \dot{f} is the rate of change of binary orbital frequency due to GW decay. The binary frequency changes by of order the starting value in a 5 year window at approximately the location of the knee feature for the ejected and 2-body BBH populations. BBHs to the left of the knee can still be detected by LISA, but will change in frequency only by the small amount indicated by the top x-axis. While these systems will not merge during the LISA lifetime, they still will have measurable orbital parameters, and might still merge while a future ground-based instrument is operating.

2.2.1 Signal-to-noise ratios

The tracks of characteristic strain in Figures 2 and 3 give a by-eye estimate of the S/N for the drawn LISA and LIGO sensitivity curves (see e.g., Cornish & Robson 2018; Moore et al. 2015). Here we quantify this, computing the S/N in the LISA and LIGO bands

as,

$$\left(\frac{S}{N}\right)^2 \approx 2 \sum_{n=1}^{n_{\text{max}}} \int_{f_{\text{start}}}^{f(\tau)} \frac{\mathcal{F}(f)h_{c,n}^2(f) df}{fP_n(f)}, \quad (6)$$

where the summation is over the relevant harmonics for an eccentric orbit (e.g., O’Leary et al. 2009). The lower limit of integration $f_{\text{start}} = nf_{\text{orb}}(0)/(1+z)$ is the GW frequency being emitted at the n^{th} harmonic of the orbital frequency when LISA or LIGO begin observation, and $f(\tau)$ is either the GW frequency at merger, or the GW frequency in the n^{th} harmonic of the orbital frequency to which the binary evolves after observation time τ . $P_n(f)$ is the noise power spectral density of the detector and $\mathcal{F}(f)$ is the detector-dependent sky and polarization averaged signal response function. For an interferometer with perpendicular arms like LIGO, $\mathcal{F}(f) = 1/5$. For LISA, $\mathcal{F}(f)$ is generally frequency dependent and is given as a fitting formula in Cornish & Robson (2018). We note that, following convention, the sensitivity curves drawn here for LIGO are simply $\sqrt{fP_n(f)}$, whereas those drawn here for LISA are $\sqrt{fP_n(f)/\mathcal{F}(f)}$.

To find $f(\tau)$ we solve the coupled ordinary differential equations for de/dt and df_{orb}/dt . We first evolve a BBH from its initial orbital frequency and eccentricity to the orbital frequency and eccentricity corresponding to the GW frequency f_{start} , at the beginning of observation. We then evolve the binary parameters for a rest-frame lifetime of $\tau/(1+z) = 5/(1+z)$ yrs and truncate at merger if necessary.

Figure 4 presents the LISA S/N for both the ejected and 2-body populations as a function of the starting $30 + 30M_{\odot}$ BBH GW frequency when LISA turns on. We consider three different redshifts to the source, our fiducial $z = 0.1$ (500 Mpc), $z = 0.3$, and $z = 0.6$. The shape of this curve can be understood partly from the shape of the LISA sensitivity curve, decreased sensitivity for frequencies departing from $\approx 10^{-2.5}$ Hz, and partly from the observation-time dependence of the characteristic strain.

For BBHs at starting frequencies to the left of the peak S/N in Figure 4, the change in binary frequency over the LISA lifetime τ is approximately zero (see the top x-axis of Figure 3). Then the integral over f can be replaced by multiplication by Δf and the S/N becomes

$$\left(\frac{S}{N}\right)^2 \propto \frac{\mathcal{F}(f)h^2(f)}{P_n(f)} \frac{f^2 \Delta f}{f} \approx \frac{\mathcal{F}(f)h^2(f)}{P_n(f)} f\tau, \quad (7)$$

which increases with increasing GW frequency as more cycles can be accumulated in an observation time. For BBHs at starting frequencies to the right of the peak S/N the binary now evolves significantly in a LISA observation time and the S/N drops with increasing frequency because GW-driven BBHs spend fewer cycles at higher frequencies. We note that the S/N calculations presented in Figure 4 are relevant for source detection only. For the measurement of eccentricity, a fisher matrix approach has been applied in Nishizawa et al. (2016) and Gondán et al. (2018). Furthermore, Nishizawa et al. (2017) has considered the ability to select formation models in addition to parameter estimation.

The frequency of maximum S/N occurs approximately where the inspiral time of a BBH equals the mission lifetime. Hence, we estimate the binary orbital eccentricity at this frequency as it signifies the highest S/N systems, and also delineates between BBHs that would be observable over the duration of a joint LISA and ground-based mission, and those that stay in the LISA band. The peak S/N occurs at

$$f([S/N]_{\text{max}}) \approx 10^{-1.8} \text{Hz} \left(\frac{\tau}{5\text{yr}}\right)^{-3/8} \left(\frac{M}{26} \frac{1+z}{1+0.1}\right)^{-5/8}, \quad (8)$$

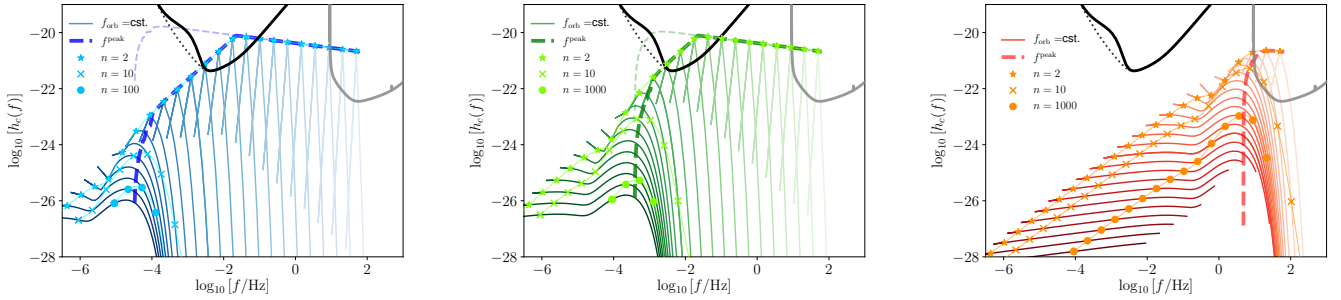


Figure 2. The tracks of eccentric $30 + 30M_{\odot}$ BBHs through GW frequency space. The BBHs are assumed to be at a distance of 500 Mpc. The three panels show tracks for each of the three populations discussed in the text; ejected (left), 2-body (center), and 3-body (right). The thick black line is the LISA instrument sensitivity curve with (solid) and without (dotted) the galactic binary background (Cornish & Robson 2018). The grey line is the advanced LIGO design-sensitivity curve (LIGO Scientific Collaboration et al. 2015). For each population (each color set / panel) the solid lines represent the GW emission at a specific binary orbital frequency, at one slice in binary-rest-frame time. The lines of constant orbital frequency are shaded dark to light for early to late time evolution. Early in the evolution, the binary is eccentric and emits at a spread of GW frequencies, with the most power at frequency f^{peak} ; evolution at f^{peak} is drawn as a thick dashed line. As the binary circularizes, it emits at predominately the $n = 2$ harmonic which is the power law that the dashed line reaches at high GW frequencies. The thin dashed lines show the characteristic strain for an infinite observation time (see text). The over-plotted, brighter markers track only single harmonics of the binary evolution. The ‘*’s track the $n = 2$ harmonic that dominates upon circularization, the ‘x’'s and the filled circles denote higher order harmonics as labeled. We compute the first 100,000 harmonics in order to draw the lines of constant orbital frequency.

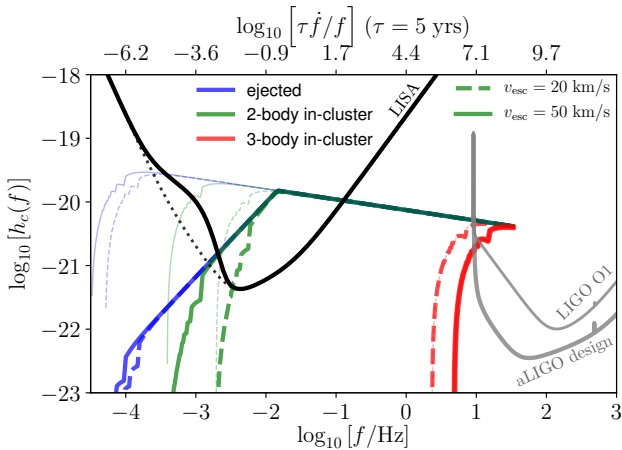


Figure 3. Tracking only the peak GW frequency of each population (thick dashed lines in Fig. 2), assuming a BBH distance of 500 Mpc. Solid lines denote representative BBHs coming from a globular cluster with an escape velocity of $v_{\text{esc}} = 50$ km/s. Dashed lines assume $v_{\text{esc}} = 20$ km/s. Different globular cluster escape velocities result in a different initial orbital frequency and eccentricity distribution for a given population. On the top x-axis, we show the ratio of the number of binary orbits that a binary will undergo in a LISA mission lifetime of $\tau = 5$ years divided by the number of orbits needed for the binary to evolve by of order its starting frequency. Labeled sensitivity curves are plotted for reference.

where we have assumed that $e \ll 1$ at the S/N peak location. At the rest-frame orbital frequency corresponding to this peak GW frequency, the binary orbital eccentricities at peak S/N are labeled for each population in Figure 4. We find that, using the average initial orbital frequencies and eccentricities of each population, the average eccentricities at peak S/N are $e([S/N]_{\text{max}}) \approx 8 \times 10^{-4}$ for the ejected population and $e([S/N]_{\text{max}}) \approx 0.01$ for the 2-body BBHs, with weak redshift dependence for $z \lesssim 1$.

We draw a vertical dotted line in Figure 1 to indicate the frequency of the peak S/N for a fiducial redshift of $z = 0.1$. From this we can visually track the BBH evolution from detection to when it leaves the LISA band. By the time the representative ejected BBH leaves the LISA band at a GW frequency of ~ 0.1 Hz, its eccen-

tricity will decay to a ~ 10 times smaller value of $e \sim 10^{-4}$. The representative 2-body BBHs, exit the LISA band with an eccentricity of $e \sim 10^{-3}$. Hence, based on estimates for LISA’s ability to measure eccentricity (Nishizawa et al. 2016, 2017; Seto 2016), we find that the eccentricity of BBHs from the 2-body population is measurable by LISA for the entire time that they are detectable in the LISA band. In contrast, the ejected BBH population has marginally measurable eccentricity only at the earliest point in its detectable evolution through the LISA band.

Figure 4 shows not only that the ejected and 2-body BBHs can be detected by LISA, but also that they will have similar detection probabilities given that they have nearly the same expected S/N in LISA. This is important for inferring the fraction of each in an observationally unbiased manner from eccentricity measurements (see, e.g., Nishizawa et al. 2017).

For the 3-body population, the relevant S/N measurement is in the LIGO band. We compute the expected S/N for the LIGO sensitivity that detected BBHs so far (approximated by the ‘Early’ curve from Abbott et al. 2018), and the aLIGO design sensitivity (LIGO Scientific Collaboration et al. 2015). For the current LIGO sensitivity curve (denoted O1 in Figure 3) we find $S/N \sim 5$ for both the 3-body BBH mergers (entering LIGO at $e \sim 0.1$) and a BBH on a circular orbit, each made of two $30M_{\odot}$ BHs at $z = 0.1$. Note that we use the sky and polarization averaged S/N to compute this value ($\mathcal{F} = 1/5$ in Eq. 6). For the aLIGO design sensitivity we find a large improvement; the representative 3-body BBH will have $S/N = 40$ in the LIGO band, approximately the same as its circular-orbit counterpart. The design sensitivity aLIGO S/N drops to a value of 8 for the 3-body BBHs at a redshift of $z = 0.32$. The prospects for measuring eccentricity for this population was studied in Tai et al. (2014) and Gondán et al. (2018).

In this section we have shown that LISA can marginally detect the eccentricity of the ejected BBHs for the first portion of their evolution in the LISA band and importantly, that LISA can observe the eccentricity decay of the 2-body BBHs over the $\lesssim 5$ years that they spends in the LISA band. After leaving the LISA band, each BBH population will have a short $\sim 11(1+z)$ day decay to merger that will pass the BBH through the DECIGO and LIGO bands.

The 3-body BBH population is not observable in the LISA band (unless they are very close so that lower harmonics pass the

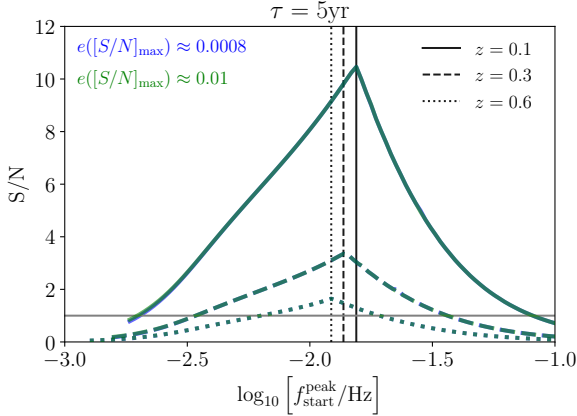


Figure 4. LISA signal-to-noise ratio for BBHs from the ejected (blue) and 2-body (green) populations, at different redshifts (the S/N is nearly identical for both populations). The x axis varies the peak GW frequency being emitted by the binary at the beginning of LISA observations, $f_{\text{start}}^{\text{peak}}$. The black vertical lines are drawn at the position of maximum S/N for each redshift. Labeled in the same colors as the corresponding BBH population are eccentricities at the value of f_{start} where the S/N is maximum in the LISA band (not greatly changing over the redshift range considered here). The black lines also indicate the GW peak frequency above which the BBHs in the ejected and 2-body populations will merge during the assumed 5 year LISA mission.

LISA S/N). As pointed out in other recent works (Rodríguez et al. 2017; Samsing et al. 2018a; Samsing & D’Orazio 2018), however, Figures 2 and 3 and our calculation of the S/N conclude that the 3-body population is detectable by LIGO, and should also be detectable as a highly eccentric source in a future DECIGO-like mission (Chen & Amaro-Seoane 2017; Samsing et al. 2018a). Figure 1 shows that this population also has an eccentricity $e \sim 0.1$ upon entering the LIGO band, which should be easily measurable (e.g., Gondán et al. 2018). Such a highly eccentric population in the LIGO band could also be created by the Kozai-Lidov mechanism (Antonini & Perets 2012; Hoang et al. 2018; Randall & Xianyu 2018b,a; Silsbee & Tremaine 2017) or GW capture from single+single interactions (O’Leary et al. 2009; Kocsis & Levin 2012; Gondán et al. 2017) in nuclear star clusters. However, these formation channels may have other unique properties that would allow future GW observations to distinguish between the two, for example correlations between BBH chirp mass and eccentricity.

3 STOCHASTIC GRAVITATIONAL WAVE BACKGROUND

Apart from individually resolvable sources in the LISA band, there will be many more binaries contributing weaker signals to a present day stochastic background of gravitational waves, which manifests as a low amplitude confusion noise for LISA.

The gravitational wave background (GWB) encodes information on an entire population of GW sources (see Rosado 2011, for a review). For binary systems, this information depends not only on the number density and distribution of BBH orbital parameters over cosmic time, but also the mechanisms which drive the binaries together. For example, previous works have considered the GWB of the most massive BBHs ($\gtrsim 10^9 M_\odot$) at the ends of their inspirals (e.g., Sesana et al. 2008, 2009; Sesana 2013; McWilliams et al. 2014), which is a prime target of the Pulsar Timing Arrays

(PTAs Lommen 2012) at low frequencies (10^{-9} Hz). These studies have shown that the inclusion of gas driven orbital decay (Kocsis & Sesana 2011), stellar scattering (Rasskazov & Merritt 2017), binary stalling (Dvorkin & Barausse 2017), significant binary eccentricity (Enoki & Nagashima 2007; Huerta et al. 2015; Chen et al. 2017), or all of the above (Kelley et al. 2017) can have dramatic effects on the predicted GWB.

Sesana (2016) and Nishizawa et al. (2016) have recently shown that stellar mass BBHs will also contribute to a GWB that is most significant in the LISA band. Here we extend this calculation to include the eccentric stellar mass BBHs formed in GCs. Specifically, we compute the GWB arising from the combination of the three, cluster-formed BBH populations of Paper I and compare to a population of circular-orbit binaries representative of those that may have formed in the field. We note that the following analysis is restricted to the equal mass case, described in the introduction to Section 2, whereas the calculations in Sesana (2016) sample the BH masses from a BH mass function. However, our main results reported below are generally valid and do not directly follow from our simplified model.

The gravitational wave background for a population of eccentric binaries has characteristic amplitude (Phinney 2001; Enoki & Nagashima 2007; Huerta et al. 2015),

$$h_c^2(f) = \frac{G}{c^2} \frac{4}{\pi f} \int_0^\infty \int_0^\infty \int_0^1 \frac{d^3 n}{dz dM de_0} \frac{dE}{df_r} de_0 dM dz. \quad (9)$$

The first term under the integrand is the co-moving differential number density of BBHs per redshift z , initial eccentricity e_0 , and chirp mass M . The second term under the integrand is the energy emitted per unit rest-frame-GW frequency,

$$\frac{dE}{df_r} = \sum_{n=1}^{n_{\text{max}}} \frac{dE_n}{df_r}, \quad (10)$$

where dE_n/df_r is given by Eq. (4). At a fixed GW frequency, summing over $n = f_r/f_{\text{orb}}$ is equivalent to summing over every orbital frequency, throughout the lifetime of the binary, that contributes power at the n^{th} harmonic to GWs at frequency f_r . This can be understood graphically from Figure 2. At a given value of f (and hence z), the sum over n is the vertical sum of all of the values of h_c^2 lying along the solid lines. The result is characteristic bumps in the GWB for an initially eccentric binary (see our Figures 2 and 5, and, e.g., Chen et al. (2017)).

While the summation over n is usually carried out up to infinity, we point out that this is only valid when there is no specified orbital frequency of formation. One should sum only over harmonics up to the maximum allowed harmonic at a given GW frequency that corresponds to the initial orbital frequency $n_{\text{max}} = f/f_0$. For the values of f_0 relevant in his study, we find that in the case of the 2-body and 3-body BBHs, this correction is negligible. For example, for the ejected population, we find that summing to infinity results in a $\sim 5\%$ overestimate of the GWB at peak. Once the binaries circularize, this approximation no longer affects our results.

We note that the form of Eq. (4), which is summed to compute the GWB, is only valid for purely GW-driven decay of the binary. This is because at each value of n and f , one derives a new value of f_{orb} that contributes to f at the n^{th} harmonic. This value of f_{orb} along with $(e_0, f_{\text{orb},0})$ is used to derive the corresponding value of e at that orbital frequency via Eq. (5). Because Eq. (5) is specifically for GW-driven evolution, the derived spectrum is valid only for GW-driven evolution as well.

Additionally, Eq. (4) is only valid when the evolution time of the BBHs is shorter than the Hubble time. This assumption holds

for the 2-body and 3-body populations, but it does not generally hold for the ejected population. Future work is planned to extend the GWB calculation to include redshift dependence in the BBH evolution in order to more accurately model the GWB from the ejected population. This will also allow us to extend the GWB calculation to the possibly large number of BBHs that will not merge in a Hubble time, and are missed here and in most calculations of the GWB.

In the context of this study, where the correction for replacing n_{\max} with infinity is small, where we assume no redshift dependence in BBH evolution, and where GW decay is the only relevant binary evolution process, we use the convenient fitting formula of [Chen et al. \(2017\)](#) (their Eqs. 15 and 16) to replace all but the co-moving differential number density in our Eq. (9).

To write the co-moving differential number density, we assume that the co-moving merger rate measured by LIGO, \mathcal{R} , is the constant rate out to a redshift of $z_{\max} = 2$, and numerically derive a probability distribution for the initial orbital eccentricities, $P_i(e_0)$, from the distributions derived in Paper I,

$$\begin{aligned} \frac{d^3 n}{dz dM de_0} &= k_i \mathcal{R} \frac{dt_r}{dz} P_i(e_0) \delta(M - M_0), \\ \frac{dt_r}{dz} &= \left[H_0(1+z) \sqrt{\Omega_M(1+z)^3 + (1+z)\Omega_k + \Omega_L} \right]^{-1}, \end{aligned} \quad (11)$$

where unless specified, we take the LIGO merger rate to be $\mathcal{R} \approx 100 \text{yr}^{-1} \text{Gpc}^{-3}$, we continue to consider a distribution of BBHs with a single chirp mass M_0 , and the subscript i denotes the i^{th} formation channel, each of which makes up a fraction k_i of the entire population. We use a cosmology with $H_0 = 70 \text{kms}^{-1} \text{Mpc}^{-1}$, $\Omega_M = 0.3$, and $\Omega_L = 0.7$.

Because dE/df_r encodes the entire orbital history of a binary with initial orbital frequency $f_{\text{orb},0}$ and eccentricity e_0 , one needs only to integrate over the distribution of initial conditions $(e_0, f_{\text{orb},0}(e_0))$. These are generated in Paper I. We truncate any contribution to the GWB below the formation frequency $f_{\text{orb},0}(e_0)$ (which would be taken into account by the value of n_{\max} if we were not using $n_{\max} \rightarrow \infty$).

Then our calculation of the GWB, for the i^{th} population of BBHs, simplifies to

$$\begin{aligned} h_{c,i}^2(f) &= k_i \mathcal{R} \left(\frac{M_0}{\mathcal{M}_{fit}} \right)^{5/3} \\ &\times \int_0^{z_{\max}} \Theta \left[f - \frac{f_0}{1+z} \right] \left(\frac{1+z}{1+z_{fit}} \right)^{-1/3} \frac{dt_r}{dz} dz \\ &\times \int_0^1 P_i(e_0) h_c^2(f, e_0, f_{\text{orb},0}) de_0, \end{aligned} \quad (12)$$

where Θ is the Heaviside step function and $h_c(f, e_0, f_{\text{orb},0})$ is given by Eqs. (13)-(15) in [Chen et al. \(2017\)](#). Corresponding to this fitting formula are the values of $z_{fit} = 0.02$ and $\mathcal{M}_{fit} = 4.16 \times 10^8 M_\odot$. The total GWB is found from $h_c^2 = \sum_i k_i h_{c,i}^2$. As in Paper I, we assume a constant chirp mass of $M_0 = 60(1/2)^{6/5}$ for a $60 M_\odot$ binary with a mass ratio of unity.

3.1 GWB: Results

The fiducial GWB and its components are displayed in Figure 5. The thick orange line in Figure 5 shows the total GWB, calculated for BBHs formed in GCs, assuming a merger rate of $100 \text{Gpc}^{-3} \text{yr}^{-1}$. The shaded orange region shows the range of possible GWBs for the range of LIGO-inferred BBH merger rates

$12 - 213 \text{Gpc}^{-3} \text{yr}^{-1}$ ([Abbott et al. 2017a](#)). The components of the GWB associated with each cluster population are drawn as dashed lines of their corresponding color: ejected (blue), 2-body (green), and 3-body (red). A comparison background of circular-orbit field binaries matched to the LIGO rate is plotted as a dashed grey line, *i.e.*, the dashed grey line would be the GWB if the LIGO rate corresponds to a population of circular-orbit BBHs and the orange line is the GWB if the LIGO rate corresponds only to GC formed BBHs.

In this section we focus on the left panel of Figure 5, which is drawn for the fiducial GC parameters used in Paper I, $v_{\text{esc}} = 50 \text{km s}^{-1}$ and single BH density of 10^5pc^{-3} . In this scenario, the ejected, 2-body, and 3-body populations make up 51.2%, 46.4%, and 2.4% of the entire GC population, respectively.

The background of BBHs on circular orbits follows the expected $f^{-2/3}$ fall of with GW frequency (*e.g.*, [Phinney 2001](#); [Kocsis & Sesana 2011](#)). The main feature prevalent in the eccentric GWB background are the bumps at which the GWB rises to an equivalent circular-orbit GWB, but at lower frequencies drops below the circular-orbit GWB. The peak of these bumps occurs near the peak GW frequency associated with the average initial eccentricity of each BBH population ($f^{\text{peak}}(e_0)$). We note that the components of the GWB associated with the merging BBH populations look very similar to the GWB expected from a population with a single eccentricity and formation frequency (see [Chen et al. 2017](#)). This is because the initial distributions derived in Paper I are very narrow for each BBH population. Physically, this is because the initial binary frequency is closely tied to the binary semi-major axis at which a binary-single interaction would eject the binary from the cluster ($f_{\text{orb},0} \sim 10^{-7}$ for $v_{\text{esc}} = 50 \text{km s}^{-1}$, see Paper I). Then because the small spread of initial orbital frequencies results in a $\mathcal{T} \sim 6 \times 10^{13}$ yr lifetime for a comparable circular-orbit binary, and because we consider only the BBHs that will merge in the LIGO band, it follows that the binary eccentricity at formation must be high in order for the BBH to merge in a Hubble time (ejected, blue population), higher still for the binary to merge before another cluster interaction (2-body, green population), and even higher still to be captured and merge during a 3-body interaction (3-body, red population). The combination of the two effects selects for a very narrow range of initial binary parameters in each population. See also discussions in Section 2.1 and 4.

The GWB of cluster-formed BBHs is largely indiscernible from a population of circular-orbit BBHs above 10^{-3} Hz. At lower frequencies, the GWB exhibits two bumps due to the 2-body BBHs at 10^{-3} Hz, and the ejected BBHs at $10^{-4.5}$ Hz. These bumps occur below the LISA sensitivity curve. We explore the dependence of the location and amplitude of these bumps on GC properties in the next section.

Finally, the orange shaded region in Figure 5 shows that, for merger rates in the LIGO-inferred range that are above our fiducial value of $100 \text{Gpc}^{-3} \text{yr}^{-1}$, the GWB falls just above the minimum of the LISA sensitivity curve (consistent with the calculation for circular-orbit binaries by [Sesana \(2016\)](#) and [Nishizawa et al. \(2016\)](#)). We note, however, that we have considered only $30+30 M_\odot$ BBHs. In addition, we have not computed the S/N for a given LISA mission, which we leave to future work that will consider a more detailed calculation of the GWB.

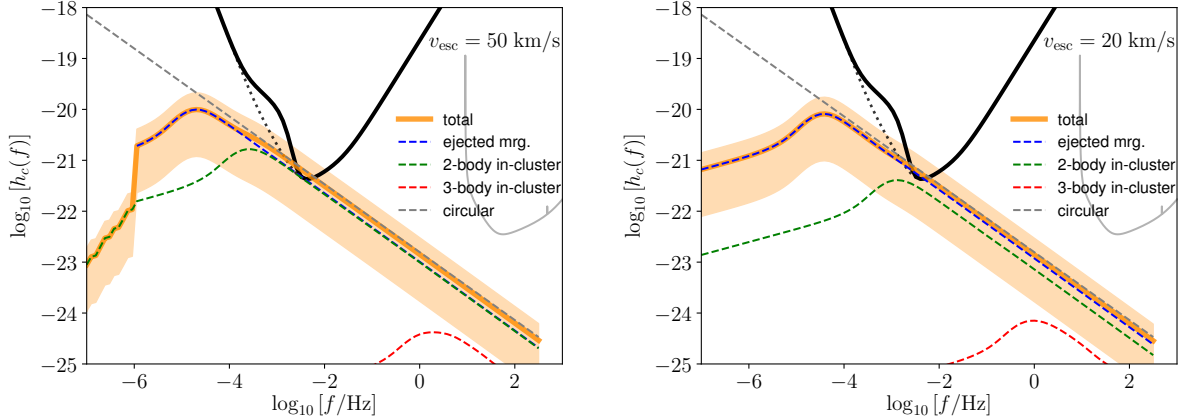


Figure 5. The gravitational wave background of cluster-formed BBHs that will merge in the LIGO band (§3). The left panel assumes GCs with an escape velocity of 50 km s^{-1} . The right panel assumes an escape velocity of 20 km s^{-1} . A merger rate of $100 \text{ Gpc}^{-3} \text{ yr}^{-1}$ is assumed with an exception for the orange shaded region, which represents the total GWB for the LIGO merger rate range $12 - 213 \text{ Gpc}^{-3} \text{ yr}^{-1}$.

4 DEPENDENCE ON GLOBULAR CLUSTER PROPERTIES

In this section we explore the dependence of our results on GC properties, focusing first on the GWB, and then applying our findings to the individually resolved sources.

As shown in §3, the main difference between a GWB composed of a dynamically-assembled eccentric population, and a canonical circular-orbit field population is the appearance of characteristic bumps, as seen in Figure 5. The location of a bump is roughly set by the frequency associated with the maximum possible pericentre distance of the considered population, which depends on the dynamical environment. It would be interesting to determine if measurements of the location of one or more of these bumps can be used to constrain the underlying BBH merger formation channel. From Figure 5, one sees that for the ejected BBH mergers (blue) the bump is generally located at frequencies too low to be observable by LISA; however, the bump for the 2-body mergers is near the region where LISA is most sensitive. In the following, we derive how the location of this 2-body-merger bump and its relative normalization depends on the underlying GC parameters.

Generally, the location of the GWB bump in frequency space will be near the minimum peak GW frequency of that population, that is the peak GW frequency at BBH formation. The reason is simply that below that frequency, the signal will not only be suppressed, but also not build up as each BBH spirals towards higher frequencies. In the following we derive how this minimum frequency, and thereby the bump location, scales for the 2-body merger population.

For the 2-body BBH mergers the minimum peak GW frequency will be the peak GW frequency emitted by a BBH with semi-major axis equal to a_{ej} and with GW inspiral life time, $\mathcal{T}(a_{ej})$ equal to the time between binary-single encounters, $t_{bs}(a_{ej})$. Using that $\mathcal{T}(a_{ej}) \approx t_c(a_{ej})(1 - e^2)^{7/2}$ (see Section 2.1 and Peters (1964)), where $t_c(a_{ej})$ refers to the BBH’s GW lifetime assuming zero eccentricity, one finds that the corresponding BBH (maximum) pericenter distance is given by $r_p/a_{ej} \approx (1/2)(t_{bs}(a_{ej})/t_c(a_{ej}))^{2/7}$. Assuming the relation $f \approx \pi^{-1} \sqrt{2Gm/r_p^3}$ presented in Eq. (1), and using that t_{bs} is the inverse of the binary-single encounter rate (e.g Samsing et al. 2018b; Samsing 2017), one now finds that the minimum peak GW frequency of the 2-body BBH merger population,

$f_{2b}^{(\min)}$, can be written as,

$$f_{2b}^{(\min)} \approx 10^{-3.5} \text{ Hz} \left(\frac{m}{30M_\odot} \right)^{2/7} \left(\frac{v_{\text{esc}}}{50 \text{ km s}^{-1}} \right)^{-12/7} \left(\frac{n_s}{10^5 \text{ pc}^{-3}} \right)^{3/7}. \quad (13)$$

To estimate the true location of the bump one has to further include the redshift distribution of the merging BBHs, their assembly eccentricity distribution, and how they merge inside their cluster. In our case one finds that the bump is just a bit above the corresponding $f_{2b}^{(\min)}$, as most of the 2-body BBHs indeed merge when their semi-major axis is $\approx a_{ej}$ (this is where $t_{bs} \propto 1/a_{ej}$ is at its maximum and $\mathcal{T} \propto a_{ej}^4$ is at its minimum), and most of the sources that give rise to the highest signal are relative nearby.

As a result, from the relation given by Eq. (13) one concludes that the 2-body population bump will move to the right when v_{esc} decreases and m, n_s increase. As the mass term m is not expected to change more than of order unity and the corresponding bump location only scales $\propto m^{2/7}$, one finds that the location is effectively a measure of v_{esc} and n_s , that is the underlying cluster properties.

The relative number of ejected mergers and 2-body mergers will also change with m, v_{esc} and n_s . To see how, we now derive an approximate relation between the expected number of 2-body mergers and ejected mergers, N_{2b}/N_{ej} . For this, we first use that the probability for a BBH to undergo a 2-body merger inside the cluster is $P_{2b} \approx P_{2b}(a_{ej})/(1 - \delta)$, where $P_{2b}(a_{ej})$ is the probability that a BBH with semi-major axis a_{ej} will merge before the next binary-single encounter, and $\delta \approx 7/9$ is the average fractional decrease in semi-major axis as a result of a hardening binary-single interaction, as further explained in Samsing (2017). The number of ejected mergers relate to the probability for an ejected BBH to merge within a Hubble time, $P_H \approx (t_H/t_c(a_{ej}))^{2/7}$. As $N_{2b}/N_{ej} \approx P_{2b}/P_H$, one now finds,

$$\frac{N_{2b}}{N_{ej}} \approx 0.8 \times \left(\frac{m}{30M_\odot} \right)^{-4/7} \left(\frac{v_{\text{esc}}}{50 \text{ km s}^{-1}} \right)^{6/7} \left(\frac{n_s}{10^5 \text{ pc}^{-3}} \right)^{-2/7}. \quad (14)$$

This relation shows how the normalizations of the GWB from the 2-body population (characterized by a bump in the LISA band) and the ejected BBH mergers (indistinguishable from simple power-law in the LISA band) scale relative to each other.

Comparing the relation describing the bump location from Eq.

(13), and the expression for the relative number of 2-body mergers given by Eq. (14), one concludes that any variation in m , v_{esc} , n_s that would move the bump towards higher frequencies into the LISA sensitivity region, also will decrease the relative number of 2-body mergers. This behavior can clearly be seen by comparing the panels in Figure 5, which present the GWB for a GC with $v_{\text{esc}} = 50 \text{ km s}^{-1}$ (left) and $v_{\text{esc}} = 20 \text{ km s}^{-1}$ (right). The smaller escape velocity example causes the GWB bump from the 2-body population to fall directly in the most sensitive frequency range for LISA, but the smaller escape velocity also diminishes the impact of the 2-body population on the GWB.

This implies, at least in our model, that it will become harder to observe the bump the more it moves towards the frequency range to which LISA is most sensitive. This complicates using the spectral shape of the GWB to constrain the underlying BBH merger progenitor channel. However, it is worth investigating more accurate dynamical models to determine if this results holds.

The above explanation for the GC-dependent location of the bumps in the GWB applies also to the tracks of individually resolvable BBHs. Figure 3 shows the evolution of the three BBH populations at the peak GW frequency for two different GC escape velocities, $v_{\text{esc}} = 50 \text{ km s}^{-1}$ (solid line) and $v_{\text{esc}} = 20 \text{ km s}^{-1}$ (dashed line). As expected from Eq. (13), the lower GC escape velocity causes the 2-body BBH populations to emit at higher peak GW frequency than for the BBHs from higher escape velocity GCs. The reason is that the BBHs in a lower escape velocity GC will be ejected at a larger semi-major axis and hence must attain a larger eccentricity in order to merge within the cluster. Higher eccentricity implies a higher peak GW frequency. A similar argument holds for the ejected population. The result, as seen in Figure 3, is that the ejected and 2-body BBHs from the lower escape velocity GC have higher initial peak GW frequencies, and hence circularize later.

The 3-body BBH mergers in Figure 3 and 5, however, shows the opposite behavior; lower escape velocity GCs produce, on average, relatively more eccentric 3-body mergers centered at lower frequencies. The reason for the relative rate increase relates to how the number of mergers contributing to each population scales with, in this case, the escape velocity v_{esc} . Following Samsing (2017), the number of ejected mergers $\propto v_{\text{esc}}^{16/7}$, the number of 2-body mergers $\propto v_{\text{esc}}^{22/7}$, where the number of 3-body mergers $\propto v_{\text{esc}}^{10/7}$. All three populations therefore decreases in number with decreasing v_{esc} , but the 3-body mergers decrease more slowly, which leads to the observed relative increase compared to the two other populations. Regarding the location at lower frequencies, this relates to the fact that the characteristic distance for two BHs to undergo a GW capture in a resonating three-body state (3-body merger) increases with the binary semi-major axis $\propto a^{2/7}$, as derived in Samsing et al. (2014); Samsing (2017). A lower v_{esc} therefore leads to 3-body mergers to generally form at larger pericenter distances, which also moves the population to lower GW peak frequencies at formation.

5 CONCLUSIONS

We have examined the GW signatures of BBHs formed dynamically in GCs. In Paper I of this series we presented three different formation channels for dynamically formed BBHs that lead to three different BBH populations identifiable by their eccentricities. Here we have computed the GW amplitude and eccentricity evolution of representative BBHs from each population, as well as a stochastic GW background from the entire population.

In order of increasing eccentricity at formation, the three merger populations are ‘ejected mergers’, ‘2-body mergers’, and ‘3-body mergers’, where the ejected and the 2-body mergers each contribute equally to the observable rate, while the 3-body mergers contribute up to $\sim 5\%$. The ejected mergers originate, as their name suggests, from BBHs that after $O(20)$ binary-single scatterings have been ejected from their cluster through a dynamical recoil. Those ejected with $e \gtrsim 0.85$ will merge in a Hubble time, and therefore contribute to the observable rate. The 2-body mergers, in contrast, merge inside the cluster, in-between hardening binary-single interactions before ejection can take place. These mergers will generally have $e \gtrsim 0.99$ at formation. The 3-body mergers form with even higher eccentricities near $e \gtrsim 0.9999$, as they are assembled during the hardening binary-single interactions.

The ejected BBHs emit GWs at $\sim 10^{-4.5}$ Hz at formation, just below frequencies at which LISA is sensitive. The 2-body BBHs form with GW frequency $\sim 10^{-3}$ Hz, directly in the LISA band, and the 3-body BBHs form at ~ 1 Hz, in-between the LISA and LIGO bands.

For a 5-year LISA mission, we quantify the properties of the ejected and 2-body BBHs that will appear in the LISA band and merge in the LIGO band. $30 + 30M_{\odot}$ BBHs at a distance of 500 Mpc, that will merge in ~ 5 yrs, are detectable with a signal-to-noise of ≈ 10 in LISA starting at a GW frequency of $\sim 10^{-1.8}$ Hz. At this frequency the average ejected BBH has an eccentricity of $e \sim 8 \times 10^{-4}$ while the average 2-body BBH has an eccentricity of $e \sim 10^{-2}$. Because LISA can measure eccentricities above $\sim 10^{-3}$ (Nishizawa et al. 2016), and because the eccentricity distribution of both populations does not significantly overlap at this GW frequency (Paper I), this means that the 2-body and ejected populations will be discernible by LISA, via their eccentricities (see Nishizawa et al. 2017). Furthermore, LISA will be able to watch the eccentricity of the 2-body BBHs evolve by an order of magnitude as they leave the LISA band, at ~ 0.1 Hz. In contrast, the ejected population has eccentricities marginally detectable by LISA when leaving the band.

The 3-body population cannot be detected by LISA, which is a clue to BBH formation on its own (Samsing et al. 2018a). However, the 3-body BBHs will enter the LIGO band with a significant eccentricity of $e \sim 0.1$. We have shown here that despite their eccentricity, these BBH systems should be detectable in advanced LIGO, and also could have been detected by LIGO O1. That no eccentric BBHs were detected in LIGO O1 and O2 is consistent with this population making up only $\sim 5\%$ of dynamically formed BBHs (Samsing 2017). Future LIGO observations will begin to constrain the fraction of BBHs that are formed dynamically. A detection of highly eccentric BBHs making up $\lesssim 5\%$ of BBH mergers in LIGO would lend significant evidence towards the BBH formation picture presented in Paper I and in other works (e.g., Samsing 2017; Rodriguez et al. 2017).

We compute the gravitational wave background (GWB) generated by the eccentric GC-formed BBHs. We find characteristic bumps in the eccentric GWB, the GW frequency of which depends most strongly on the GC escape velocity. While low escape velocity clusters cause such a GWB bump from the 2-body population to fall directly in the LISA band, the same low escape velocity clusters also cause the GWB due to ejected mergers to dominate over the 2-body GWB. Hence the GWB is very similar to that found for BBHs on circular orbits formed in the field (e.g., Sesana 2016; Nishizawa et al. 2016). In any case, the GWB is marginally detectable for the fiducial BBH populations considered here.

As we have shown, the GW signatures of eccentric BBHs

formed in GCs provide a powerful tool for deciphering the origin of BBH systems, a tool uniquely suited for multi-band GW astronomy of the coming decade. In future work we plan to expand upon the schematic calculation of the GWB presented here. Specifically, we wish to extend our calculation to more accurately capture the GWB from the ejected populations, and to the BBHs that stall, with a range of eccentricities below that needed to merge. To achieve this one must adapt the commonly used expression for the GWB strain (Eq. 9), to include BBH evolution on a timescale that is comparable to the Hubble time. Additionally, a more accurate representation of the distribution of chirp masses and the redshift distribution must be included, not only for the GWB calculation but most importantly to estimate the number and orbital parameter distribution of BBHs that LISA and LIGO will detect.

ACKNOWLEDGEMENTS

We thank the referee, Emanuele Berti, for constructive suggestions that enhanced the quality of this work. We thank Alberto Sesana and Bence Kocsis for helpful discussions pertaining to LISA and the signal-to-noise estimates. Financial support was provided from NASA through Einstein Postdoctoral Fellowship award number PF6-170151 (D.J.D.) and from the Lyman Spitzer Fellowship (J.S.).

References

- Abbott B. P., et al., 2016a, *Physical Review X*, **6**, 041015
 Abbott B. P., et al., 2016b, *Physical Review Letters*, **116**, 061102
 Abbott B. P., et al., 2016c, *Physical Review Letters*, **116**, 221101
 Abbott B. P., et al., 2016d, *Physical Review Letters*, **116**, 241102
 Abbott B. P., et al., 2016e, *Physical Review Letters*, **116**, 241103
 Abbott B. P., et al., 2016f, *ApJL*, **818**, L22
 Abbott B. P., et al., 2017a, *Physical Review Letters*, **118**, 221101
 Abbott B. P., et al., 2017b, *Physical Review Letters*, **119**, 141101
 Abbott B. P., et al., 2017c, *ApJL*, **851**, L35
 Abbott B. P., et al., 2018, *Living Reviews in Relativity*, **21**, 3
 Amaro-Seoane P., Santamaría L., 2010, *ApJ*, **722**, 1197
 Amaro-Seoane P., et al., 2017, preprint, ([arXiv:1702.00786](https://arxiv.org/abs/1702.00786))
 Antonini F., Perets H. B., 2012, *ApJ*, **757**, 27
 Barack L., Cutler C., 2004, *PRD*, **70**, 122002
 Belczynski K., et al., 2017, preprint, ([arXiv:1706.07053](https://arxiv.org/abs/1706.07053))
 Benacquista M. J., 2002, *Classical and Quantum Gravity*, **19**, 1297
 Breivik K., Rodríguez C. L., Larson S. L., Kalogera V., Rasio F. A., 2016, *ApJL*, **830**, L18
 Chen X., Amaro-Seoane P., 2017, *ApJL*, **842**, L2
 Chen S., Sesana A., Del Pozzo W., 2017, *MNRAS*, **470**, 1738
 Cholis I., Kovetz E. D., Ali-Haïmoud Y., Bird S., Kamionkowski M., Muñoz J. B., Raccanelli A., 2016, *PRD*, **94**, 084013
 Cornish N., Robson T., 2018, preprint, ([arXiv:1803.01944](https://arxiv.org/abs/1803.01944))
 Dvorkin I., Barausse E., 2017, *MNRAS*, **470**, 4547
 Enoki M., Nagashima M., 2007, *Progress of Theoretical Physics*, **117**, 241
 Farr W. M., Stevenson S., Miller M. C., Mandel I., Farr B., Vecchio A., 2017, *Nature*, **548**, 426
 Farr B., Holz D. E., Farr W. M., 2018, *ApJL*, **854**, L9
 Fishbach M., Holz D. E., Farr B., 2017, *ApJL*, **840**, L24
 Fregeau J. M., Larson S. L., Miller M. C., O’Shaughnessy R., Rasio F. A., 2006, *ApJL*, **646**, L135
 Gerosa D., Berti E., 2017, *PRD*, **95**, 124046
 Gerosa D., Kesden M., Berti E., O’Shaughnessy R., Sperhake U., 2013, *PRD*, **87**, 104028
 Gerosa D., Kesden M., Sperhake U., Berti E., O’Shaughnessy R., 2015, *PRD*, **92**, 064016
 Gondán L., Kocsis B., Raffai P., Frei Z., 2017, preprint, ([arXiv:1711.09989](https://arxiv.org/abs/1711.09989))
 Gondán L., Kocsis B., Raffai P., Frei Z., 2018, *ApJ*, **855**, 34
 Gültekin K., Miller M. C., Hamilton D. P., 2006, *ApJ*, **640**, 156
 Hoang B.-M., Naoz S., Kocsis B., Rasio F. A., Dosopoulou F., 2018, *ApJ*, **856**, 140
 Huerta E. A., McWilliams S. T., Gair J. R., Taylor S. R., 2015, *PRD*, **92**, 063010
 Kawamura S., et al., 2011, *Classical and Quantum Gravity*, **28**, 094011
 Kelley L. Z., Blecha L., Hernquist L., Sesana A., Taylor S. R., 2017, *MNRAS*, **471**, 4508
 Kesden M., Gerosa D., O’Shaughnessy R., Berti E., Sperhake U., 2015, *Physical Review Letters*, **114**, 081103
 Kocsis B., Levin J., 2012, *PRD*, **85**, 123005
 Kocsis B., Sesana A., 2011, *MNRAS*, **411**, 1467
 LIGO Scientific Collaboration et al., 2015, *Classical and Quantum Gravity*, **32**, 074001
 Lehner L., Pretorius F., 2014, *ARA&A*, **52**, 661
 Lommen A. N., 2012, *Journal of Physics Conference Series*, **363**, 012029
 Luo J., et al., 2016, *Classical and Quantum Gravity*, **33**, 035010
 McWilliams S. T., Ostriker J. P., Pretorius F., 2014, *ApJ*, **789**, 156
 Moore C. J., Cole R. H., Berry C. P. L., 2015, *Classical and Quantum Gravity*, **32**, 015014
 Nishizawa A., Berti E., Klein A., Sesana A., 2016, *PRD*, **94**, 064020
 Nishizawa A., Sesana A., Berti E., Klein A., 2017, *MNRAS*, **465**, 4375
 O’Leary R. M., Kocsis B., Loeb A., 2009, *MNRAS*, **395**, 2127
 Park D., Kim C., Lee H. M., Bae Y.-B., Belczynski K., 2017, *MNRAS*, **469**, 4665
 Peters P. C., 1964, *Physical Review*, **136**, 1224
 Peters P. C., Mathews J., 1963, *Physical Review*, **131**, 435
 Phinney E. S., 2001, ArXiv Astrophysics e-prints,
 Portegies Zwart S. F., McMillan S. L. W., 2000, *ApJL*, **528**, L17
 Randall L., Xianyu Z.-Z., 2018a, preprint, ([arXiv:1802.05718](https://arxiv.org/abs/1802.05718))
 Randall L., Xianyu Z.-Z., 2018b, *ApJ*, **853**, 93
 Rasskazov A., Merritt D., 2017, *PRD*, **95**, 084032
 Rodríguez C. L., Chatterjee S., Rasio F. A., 2016a, *PRD*, **93**, 084029
 Rodríguez C. L., Zevin M., Pankow C., Kalogera V., Rasio F. A., 2016b, *ApJL*, **832**, L2
 Rodríguez C. L., Amaro-Seoane P., Chatterjee S., Rasio F. A., 2017, preprint, ([arXiv:1712.04937](https://arxiv.org/abs/1712.04937))
 Rosado P. A., 2011, *PRD*, **84**, 084004
 Samsing J., 2017, preprint, ([arXiv:1711.07452](https://arxiv.org/abs/1711.07452))
 Samsing J., D’Orazio D. J., 2018, preprint, ([arXiv:1804.06519](https://arxiv.org/abs/1804.06519))
 Samsing J., Ilan T., 2017, preprint, ([arXiv:1709.01660](https://arxiv.org/abs/1709.01660))
 Samsing J., Ilan T., 2018, *MNRAS*, **476**, 1548
 Samsing J., Ramirez-Ruiz E., 2017, *ApJL*, **840**, L14
 Samsing J., MacLeod M., Ramirez-Ruiz E., 2014, *ApJ*, **784**, 71
 Samsing J., D’Orazio D. J., Askar A., Giersz M., 2018a, preprint, ([arXiv:1802.08654](https://arxiv.org/abs/1802.08654))
 Samsing J., MacLeod M., Ramirez-Ruiz E., 2018b, *ApJ*, **853**, 140
 Samsing J., Askar A., Giersz M., 2018c, *ApJ*, **855**, 124
 Sesana A., 2013, *MNRAS*, **433**, L1
 Sesana A., 2016, *Physical Review Letters*, **116**, 231102
 Sesana A., Haardt F., Madau P., Volonteri M., 2005, *ApJ*, **623**, 23
 Sesana A., Vecchio A., Colacino C. N., 2008, *MNRAS*, **390**, 192
 Sesana A., Vecchio A., Volonteri M., 2009, *MNRAS*, **394**, 2255
 Seto N., 2016, *MNRAS*, **460**, L1
 Silsbee K., Tremaine S., 2017, *ApJ*, **836**, 39
 Tai K. S., McWilliams S. T., Pretorius F., 2014, *PRD*, **90**, 103001
 Wen L., 2003, *ApJ*, **598**, 419
 Yunes N., Yagi K., Pretorius F., 2016, *PRD*, **94**, 084002
 Zevin M., Pankow C., Rodríguez C. L., Sampson L., Chase E., Kalogera V., Rasio F. A., 2017, *ApJ*, **846**, 82

This paper has been typeset from a $\text{\TeX}/\text{\LaTeX}$ file prepared by the author.